Research Article

Modelling Hydrodynamic Changes in the Salinity of the Hammar Marsh and Shatt al-Arab Waters Using Dimensional Analysis and Remote Sensing

Forqan Khalid Al-Daraji[1], Husam Hasan Abdulaali[2*], Yousif Sh. J. Al-Jorani and Muayad H. M. Albehadili[1]

[1]Department of Applied Marine Sciences, College of Marine Sciences, University of Basrah, Basrah Governorate, Iraq; [2]Soil Science and Water Resources Department, Faculty of Agriculture, University of Basrah.

Abstract | Conversely, weather-related influences such as temperature and evaporation result in greater salt concentration. The biological activity by meansof the normalised difference chlorophyll index (NDCI) also influences chemical interactions as well as salt distribution. Differences in salinity. The geographical distribution and temporal variability of salinity are also dynamic. This was derived from simulated data on April 5 and 18, 2024. Differences in the rate of change were observed between areas near the water source (upstream) and far from it (downstream). The research emphasises the significance of a combined approach of field-based data and remote sensing to improve mathematical models for decision support in water resources management in southern Iraq. This site is located on the alluvial plain of northern Basrah Governorate, Iraq.

Received | January 07, 2026; **Accepted** | January 26, 2026; **Published** | March 26, 2026
***Correspondence** | Husam Hasan Abdulaali, Soil Science and Water Resources Department, Faculty of Agriculture, University of Basrah; **Email:** husam.abdulaali@uobasrah.edu.iq
Citation | Al-Daraji, F.K., H.H. Abdulaali, Y.S.J. Al-Jorani and M.H.M. Albehadili. 2026. Modelling hydrodynamic changes in the salinity of the Hammar Marsh and Shatt Al-Arab waters using dimensional analysis and remote sensing. *Pakistan Journal of Agricultural Research,* 39(1): 203-214.
DOI | https://dx.doi.org/10.17582/journal.pjar/2026/39.1.203.214
Keywords | Water salinity, Remote sensing, Dimensional analysis, World heritage sites, Climate change

Introduction

The Shatt al-Arab River and the marshlands of southern Iraq are important natural features that have heavily influenced the region's historical environmental and social identity, owing to their economic and heritage significance (Qadra, 2020). The Shatt al-Arab River, created by the confluence of the Tigris and Euphrates rivers north of Basrah at Qurna. It runs for about 200 km before it empties into the Arabian Gulf (Danboos *et al.*, 2023). It functions as an important channel for trade and irrigation, thereby increasing farming output (Hamdan *et al.*, 2018). The Iraqi Marshes are among the largest wetlands in the Middle East. In addition, they harbour high biodiversity, serve as breeding grounds for migratory birds and fish, and provide sustenance to local communities relying on fishing and farming. These marshes were added to UNESCO's World Heritage List for their habitat-related values and cultural heritage, as well as for their association with the civilisation of Mesopotamia (Smaysim and Slewa, 2014). Yet, the marsh reeds are under increasing environmental threats, associated with both drought

and climate change, which negatively affect the hydrological regime of the Shatt al-Arab River and its discharge (Al-Jiburi and Al-Basrawi, 2009). The intake of the Shatt al-Arab into the Persian Gulf, additionally intensified by climate change (Al-Mahmood and Al-Mahmood, 2021), has significantly reduced the flow of the Tigris and Euphrates since dam construction in Turkey and Syria (Haleem and Al-Muhyi, 2018). Human interventions such as the marsh drainage campaigns of the 1990s, excessive water use, and industrial pollution have further intensified salinity challenges and complicated traditional monitoring efforts (Hamdan *et al*., 2020). Remote sensors have been a useful means of collecting real-time, accurate information from remote locations (Vijayan *et al*., 2010). Projection models help estimate future salinisation indicators and support effective monitoring of environmental degradation and its effects on agriculture and biodiversity (Saleh, 2017; Alqasemi *et al*., 2021). Salinity in the Shatt al-Arab River has increased to 10–12 ppm, clearly demonstrating the need for desalination projects and enhanced local cooperation (Hamdan *et al*., 2020). Over the last 20 years, temperatures in southern Iraq have increased by 1.5°C, while rainfall has decreased by 20% (Al-Daraji *et al*., 2025), highlighting the imperative nature of formulating successful water management strategies to address climate change (Al-Khalidi *et al*., 2018). Salinity in the marshes reaches 12 ppm, implying a growth in freshwater inflow and sound water management (Mohamed *et al*., 2016). Other research also reports a 40% decrease in streamflow (Tigris-Euphrates) resulting from the construction of dams upstream (Adamo *et al*., 2018). On the other hand, conventional water quality monitoring approaches in southern Iraq incur annual expenses exceeding $3 million, thereby calling for the application of cost-effective geomatics tools to improve data correctness (Harmel *et al*., 2023). Reported that high temperatures and scant rainfall led to a 20% increase in river salinity in southern Iraq, prompting researchers to propose improved water management to reduce the impact of climate change (Al-Salihi *et al*., 2024). Reported that water salinity resulted in a 50% drop in crop yield in some locations, and recommended advanced technologies for water management and salinity reduction (Van Zandwijk *et al*., 2021). The Shatt al-Arab, water salinity was 18.5 ppm in 2009 and was increasing further, they recommended better water management in the area. Noted that salinity in the Karma Ali River increased by 15% due to industrial and sewage pollution, and recommended the use of modern technology for controlling pollution impacts on the environment (Al-Jawad *et al*., 2018). Several investigators have monitored river water salinity using satellite data (Harmel *et al*., 2023).

A study by Ahmed *et al*. (2023) utilised Landsat and Sentinel-2 data to assess water salinity in the Tigris River at 15 locations, disclosing a strong correlation (r = 0.85) between salinity and medium-wave infrared (MWIR) data with 90% accuracy. In a study by Mukhamediev *et al*. (2023), Landsat 8 data were used to measure water salinity in the Kazakhstan River at 10 locations, achieving 85% accuracy with a moderate correlation (r= 0.72) between salinity and near-infrared (NIR) data (Li *et al*., 2021). A quantitative model for salinity was developed using visible–near-infrared spectral data processed with the Savitzky–Golay filter, MSC, and combined transformations. Spectral metrics (DI, RI, NDI) were calculated, and the most informative (Spearman's r > 0.8) were selected. Results from the RBF neural network model showed that its accuracy was relatively good (R^2= 0.950, RMSE= 1.014, RPD= 4.479) and that it could effectively predict salinity values. The combination of remote sensing (Landsat 9 and Sentinel-2 bands/salinity indices) with environmental predictors (ENVI) largely improved soil salinity estimates, whereas the RS + ENVI approach using Sentinel-2 showed the best model effectiveness (R^2 = 0.86), compared to single RS or ENVI models (Jia *et al*., 2024). A study created a multivariable linear algorithm to estimate sea surface salinity (SSS) using Landsat 8 OLI bands 1 to 4. The method achieved high accuracy (R^2= 0.74 and RMSE < 2%) even though a certain algorithm parameters and data were limited. It identified SSS changes during extreme events at higher spatial and temporal scales, whereas numerical models overestimated salinity by 3.4%, showing how high-resolution satellites can monitor small-scale marine features (Zhao *et al*., 2017). The (MPNN SSS model), constructed from both MODIS and SeaWiFS data (Rrs at 412-667 nm, SST), performed well with RMSE= 1.2, R^2= 0.86, and the bias close to zero to resolve gradients at a spatial resolution of 1 km from coastal to offshore regions in the northern Gulf of Mexico. Its reliability was assessed through validation and sensitivity tests (RMSE= 1.1 on independent data) that also showed that the obtained map, compared to Aquarius maps, had an improved ability to resolve

fine-scale features and salinity gradients. However, the application in algal bloom and upwelling areas was restricted due to interference from blue-band Rrs (Chen and Hu, 2017), reported that high levels of soil and water salinity were increasingly threatening crop productivity and quality, particularly in arid or semi-arid climates with high evaporation and intensive irrigation. They used Landsat-5 TM satellite images in their study conducted on the Neretva River Delta, Croatia, to investigate low to moderately salt-affected agricultural land. The results indicated that remotely sensed data could explain 43% and 62% of the variation in water salinity using the SLR and MLR models, respectively, suggesting the applicability of this technique for assessing environmental quality in salt-affected agricultural lands (Racetin *et al*., 2020). Reported that the saline balance conditions of the estuarine ecosystems, which are altered suddenly by storms and hurricanes, lead to disturbances in aquatic life (Wang and Xu, 2011). Although measuring salinity directly using remote sensing is challenging, studies have found a correlation between salinity, colored dissolved organic matter (CDOM) and suspended solids, allowing the development of indirect estimative models for monitoring salinity changes. Due regarding challenges in direct data collection, machine learning techniques were applied to assess salinity in East Sivash Bay using 93 in situ samples and 6 Sentinel-2 datasets. The best simple linear regression model attained an accuracy of 0.8797, while the random forest, along with AdaBoost models, showed lower accuracies. The study also found that as salinity increases, light absorption shifts to the infrared spectrum, permitting regular surveillance of hypersaline water bodies using remote sensing (Borovskaya *et al*., 2022). Established strategies commonly fail to meet the effectiveness along with exactness needs in complex basins. The USalt system is proposed to utilise UAV mobility and IR-UWB radar for fast and accurate salinity sensing. The system eliminates signal contamination and extracts salinity-related features with a neural network model (ssNet) for exact estimation. An advanced learning framework (mssNet) was developed for ecological flexibility. Field experiments have shown that USalt achieves an MAE of 0.39 g/100 mL in water salinity sensing (Wang *et al*., 2024b).A study uses Landsat 8 OLI imagery and 102 in situ salinity data points to map salinity in the Karun River, Iran. including spectral bands and salinity indices were assessed using Random Forest Variable Significance Score (RFFIS), Sobol's sensitivity analysis, and correlation with salinity. Key features for salinity estimation included the Red and Green bands, salinity indices 2-6 NSMI and EGRI. Spatial autocorrelation analysis suggested that models including spatial terms produced better results. Landsat 8 OLI effectively mapped salinity changes and increased the salinity due to agriculture (Ansari *et al*., 2025). However, the use of remote sensing-based studies with mathematical models to evaluate river salinity and improve water management in climate change is one commonality in all the articles, providing several suggestions for developing a model that includes more climatic and seasonal agents to increase forecast precision and guarantee planning for renewable water resources. The objectives are to derive a work method for integrating ground measurements and remote sensing products into a hydrodynamic mathematical model to monitor/simulate the changes in water salinity in these Al-Hamaar Marshes / Shatt al-Arab River UNESCO World Heritage site areas.

Materials and Methods

Study location

The study took place in southern Iraq, in the alluvial plain of the Mesopotamian (Wadi al-Rafidain) region, located in the northern part of Basrah Province (Sissakian *et al*., 2014). The study concentrated on the branch of the Shatt al-Arab River and the southern section of Hawr al-Himar (Al-Daraji *et al*., 2024). Samples were collected in two phases, with 40 water samples taken per phase. In each phase, 20 water samples were randomly distributed at sites whose coordinates were recorded using GPS, covering an area with a total land surface of approximately 153 km^2 and an aquatic surface (including water bodies and the river network) of about 20.51 km^2, as shown in Figure 1.

Satellite imagery and information processing

Landsat 8 satellite imagery was downloaded from the United States Geological Survey (USGS) website on April 5, 2024, and April 18, 2024. These dates correspond to the data acquisition times for each row and satellite orbit that provided a scene covering the study area. ArcGIS 10.8 software was used to perform spectral correction on the satellite imagery and to extract the targeted study area. Subsequently, digital data processing was conducted, and the spectral reflectance for bands 2 through 10 was computed (Tajudin *et al*., 2021). From these data,

the water salinity index (Al-Khakani *et al.*, 2018) and the normalised difference chlorophyll index (NDCI) were derived, both of which are considered among the most important variables in model construction (Pałas and Zawadzki, 2020).

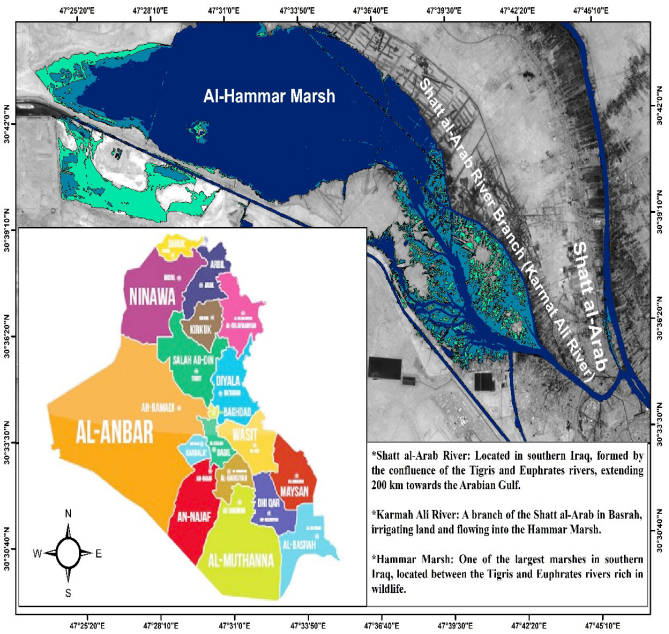

Figure 1: *Shows the study area.*

Variables and mathematical model construction

The variables were identified, and Buckingham's π-theorem was applied for the purpose of deriving the variables and obtaining the governing Equation 1 as shown in Table 1, as follows (Phull and Babar, 2012):

$$S_m = f(S\_index, NDCI, L, D, g, T, E, \rho) \quad \ldots(1)$$

Several remote sensing variables were computed as follows:

Salinity Index (Equation 2):

$$S\ index = \sqrt{Band3 * Band4} \quad \ldots.(2)$$

Band 3: Reflectance in the green wavelength range (0.53–0.59 µm), Band 4: Reflectance in the red wavelength range (0.64–0.67 µm).

Normalised Difference Chlorophyll Index (NDCI, Equation 3):

$$NDCI = \frac{(Band5 - Band2)}{(Band5 + Band2)} \quad \ldots(3)$$

Band 5: Reflectance in the Near-Infrared (NIR) range, corresponding to Band 5 in Landsat 8. Band 2: Reflectance in the Red band, corresponding to Band 2 in Landsat 8.

Evapotranspiration in the study area was calculated using remote sensing data and the Eq. developed by Al-Daraji *et al.* (2025), which is based on the modified Thornthwaite method that utilises thermal bands and satellite imagery.

Table 1: *Shows the variables of the proposed model.*

No	Variable	Variable symbol	Type of variable	Unit of measurement	Dimensions	Notes
1	Water salinity	S_m	Dependent	g L^{-3}	ML^{-3}	Measurements were conducted in the field and subsequently converted to EC ds m^{-1}
2	Water salinity index	S index	Independent	Non Unit	1	Measured by using remote sensing, Equations 2, 3
3	Normalized difference chlorophyll index in water	NDCI				
4	Distance from the main river	L		m	L	Measured from satellite images using GIS
5	Water depth	D			L	Measured in the field using a measuring wire
6	Land surface temperature	T		Celsius	θ	Measured using the remote sensing thermal equilibrium method
7	Daily evapotranspiration	Et		mm day^{-1}	LT^{-1}	Measured using remote sensing, applying the Thornthwaite method as modified by Al-Daraji *et al.* (2024)
8	Water density	ρ		kg m^{-1}	ML^{-3}	Measured in the field
9	Gravitational acceleration	g		m s^{-2}	LT^{-2}	Constant value

The number of dimensionless groups (π) is determined as follows:

The total number of variables (n) is nine, and the number of fundamental dimensions (k) is four, namely mass (M), length (L), time (T), and temperature (θ). Therefore, the number of dimensionless groups (π) is 5, according to Equation 4:

$$\pi\text{-}groups = n - k \Rightarrow 9 - 4 = 5 \quad \ldots(4)$$

The fundamental variables that cover all the basic dimensions are selected as follows: for mass (M), water density (ρ) is chosen; for length (L), the distance from the main river (L) is chosen; for time (T), gravitational acceleration (g) is selected and for temperature (θ), air temperature (T) is selected. In order to compute the exponents in each dimensionless group (π-group) using the Buckingham π-theorem, the following steps are followed:

$$\pi_1 = \frac{S_m}{\rho^a \cdot L^b \cdot g^c \cdot T^d} \quad \ldots(5)$$

$$S_m = \rho^a . L^b . g^c . T^d \quad \ldots.(6)$$

$$ML^{-3} = (ML^{-3})^a . (L)^b . (LT^{-2})^c . (\theta)^d \quad \ldots.(7)$$

Dimensional equilibrium:

$$\begin{cases} [M]: 1 = a \\ [L]: -3 = -3a + b + c \\ [T]: 0 = -2c \\ [\theta]: 0 = d \end{cases} \quad \ldots(8)$$

$$a = 1, b = 0, C = 0, d = 0$$

$$\pi_1 = \frac{S_m}{\rho} \quad \ldots(9)$$

Thus, the steps described above can be repeated to compute π_2, π_3, π_4, and π_5, as illustrated in Table 2:

Table 2: *The π-groups and their exponents.*

Exponents Variables (a, b, c, d)	π-group	Variable
a= 1, b=0, c=0, d=0	π_1= S_m/ρ	S_m
a= 0, b=0, c=0, d=0	π_2= Sindex	S index
a= 0, b=0, c=0, d=0	π_3= NDCI	NDCI
a= 0, b=1, c=0, d=0	π_4= D/L	D, L
a= 0, b= 0.5, c= 0.5, d=0	π_5= Et/√gL	Et, g

About the temperature T, it was chosen as the fundamental variable to represent the dimension (θ). However, it does not appear in the other dimensionless groups because the non-fundamental variables do not depend on temperature, which results in the temperature exponent, d, being zero in all groups for any spatial dimensions. After establishing the dimensionless groups, the final governing equations are obtained. Can be formulated as follows:

$$\pi_1 = f(\pi_2, \pi_3, \pi_4, \pi_5) \quad \ldots(10)$$

$$\frac{S}{\rho} = f\left(S\ index, NDCI, \frac{D}{L}, \frac{Et}{\sqrt{gL}}\right) \quad \ldots(11)$$

The regression analysis between the computed (S_m) values and the field values (S_f) is repeated using curve fitting with the SPSS statistical analysis program (Table 3).

Table 3: *The type of regression relationship between π-groups.*

Variable	Symbol	Regression relationship	Constants
S_m/p	π_1	-	a_0= -30.410
S index	π_2	Inverse	a_1= 0.255
NDCI	π_3	Cubic	a_2=-2.475
D/L	π_4	Exponential (ln)	a_3= -0.270
Et/√(gL)	π_5	Inverse	a_4= 141.159

$$\pi_1 = a1 \cdot \frac{1}{\pi_2} + a2 \cdot {\pi_3}^3 + a3 \cdot ln(\pi_4) + a4 \cdot \frac{1}{\pi_5} \quad \ldots.(12)$$

$$S_m = e^{a + \frac{b}{\rho.\left[(0.255).\frac{1}{S\ index} + (-2.475).(NDCI)^3 + (-0.270).Ln\left(\frac{D}{L}\right) + 141.159.\frac{Et}{gL} + (-30.410)\right]}} \quad \ldots.(13)$$

$$S_m = \rho.\left[(0.255).\frac{1}{S\ index} + (-2.475).(NDCI)^3 + (-0.270).Ln\left(\frac{D}{L}\right) + 141.159.\frac{Et}{\sqrt{gL}} + (-30.410)\right] \quad \ldots(14)$$

The governing relationship was exponential, yielding constants a= 3.698 and b= −15488.251, with a correlation coefficient of R= 0.714 (Sahbeni, 2021). Upon substituting these values into Equation 15, the final Eq. becomes as follows:

$$S_m = e^{(3.698 + \frac{-15488.251}{\rho.\left[(0.255).\frac{1}{S\ index} + (-2.475).(NDCI)^3 + (-0.270).Ln\left(\frac{D}{L}\right) + 141.159.\frac{Et}{gL} + (-30.410)\right]}} \quad \ldots(15)$$

It can be applied by employing remote sensing and establishing water salinity monitoring (in units of EC ds·m^{-1}) in the Shatt al-Arab River branch and the al-Hammar marsh.

Results and Discussion

Integration of field and satellite data in the evaluation of the aquatic system

Table 4 presents a comprehensive study that

integrates field data with satellite imagery-derived information to assess the condition of the aquatic system. The research considered two main variables: water depth (D), Normalised Difference Chlorophyll Index (NDCI), and Salinity Index (SI), along with some climate indicators: Land Surface Temperature (LST) and Evapotranspiration (ET). Coordinates and distances from the mainstream were collected for spatial analysis of the sites. Depth ranged from 0.75 to 9.00 m, and NDCI ranged between –0.22 and 0.20.

Table 4: *Shows the values of all variables included in the proposed model.*

No	Date	Coordinates		Distance from the main river	Water depth	Normalized difference chlorophyll index	Water salinity index	Evapotranspiration	Land surface temperature	Water density	Field measured water salinity
		X	Y	L (m)	D (m)	NDCI	SI Index	ET (mm day^{-1})	LST (^{o}C)	ρ (kg m^{-1})	S $_{f}$(dS m^{-1})
1	5 Apr. 24	765.43	3386.39	550.10	9.00	-0.11	0.15	1.23	24.04	1000.80	2.20
2		764.30	3385.25	2070.19	8.00	-0.10	0.15	1.76	26.00	1001.04	1.74
3		762.42	3386.25	3559.75	5.60	-0.08	0.14	1.45	24.88	1001.42	1.77
4		760.64	3387.46	5421.44	6.80	-0.09	0.14	1.29	24.27	1002.76	1.04
5		758.13	3388.08	8006.37	6.00	-0.11	0.13	1.11	23.58	1003.82	0.74
6		756.21	3389.31	10166.56	5.40	-0.20	0.12	1.03	23.27	1003.87	0.87
7		755.63	3391.08	11315.47	5.00	-0.22	0.13	1.06	23.38	1004.35	1.00
8		754.86	3392.27	12533.35	2.75	-0.19	0.16	1.04	23.31	1004.43	1.07
9		753.40	3393.98	14638.94	3.70	-0.19	0.17	1.17	23.81	1004.95	1.18
10		752.46	3395.83	16428.66	3.00	-0.19	0.17	0.95	22.95	1005.88	1.29
11		750.51	3397.65	19079.21	3.10	-0.18	0.15	1.42	24.79	1005.89	1.34
12		751.02	3398.88	19423.32	2.81	0.16	0.11	1.78	26.09	1006.54	1.39
13		748.85	3397.89	20572.24	2.61	-0.19	0.14	1.00	23.15	1006.66	1.41
14		749.35	3399.45	21078.75	1.80	0.17	0.11	1.81	26.18	1007.18	1.41
15		746.91	3397.08	21814.56	1.50	-0.20	0.15	0.92	22.82	1007.62	1.42
16		745.07	3395.86	22912.57	0.75	-0.20	0.13	0.96	22.99	1010.62	1.46
17		748.70	3401.67	22996.96	1.20	0.10	0.11	1.41	24.76	1010.85	1.57
18		746.95	3399.59	23106.73	2.30	-0.19	0.13	0.95	22.93	1011.11	1.70
19		747.50	3400.88	23415.75	1.44	-0.11	0.11	1.19	23.90	1011.66	1.80
20		743.51	3396.63	24651.01	1.47	0.02	0.11	1.32	24.40	1012.35	1.87
21	18 Apr. 24	744.79	3399.30	24760.18	2.70	-0.11	0.11	0.90	22.72	1017.29	1.94
22		746.55	3402.07	24903.60	1.60	0.12	0.11	1.34	24.46	1010.51	2.05
23		743.59	3397.95	25148.18	2.30	-0.13	0.11	0.97	23.00	1005.18	2.36
24		744.45	3400.44	25653.85	2.00	-0.06	0.12	0.96	22.98	1015.05	2.68
25		743.35	3399.49	26096.24	2.33	-0.12	0.11	0.84	22.48	1016.17	2.38
26		742.18	3397.36	26158.07	1.75	0.00	0.10	1.15	23.76	1009.48	2.02
27		745.21	3402.61	26288.36	1.40	0.02	0.10	1.18	23.86	1006.98	2.07
28		743.04	3401.35	27329.21	1.45	-0.11	0.11	0.87	22.60	1000.05	2.12
29		741.78	3400.30	27860.55	1.75	-0.05	0.11	0.89	22.71	1004.52	2.13
30		740.89	3398.81	27947.39	2.10	0.16	0.10	1.29	24.29	1002.93	2.16
31		742.15	3402.62	28778.73	1.00	0.20	0.11	1.22	24.03	1011.61	2.26
32		740.07	3400.15	29289.34	2.10	-0.20	0.11	0.84	22.47	1017.66	2.37
33		740.74	3401.98	29607.71	3.40	-0.15	0.10	0.83	22.42	1005.61	2.46
34		738.86	3399.20	29943.88	2.78	-0.07	0.09	0.96	22.99	1004.33	2.52
35		740.24	3403.39	30791.39	1.60	0.06	0.12	1.10	23.54	1015.81	2.53
36		737.53	3398.40	30841.68	3.00	-0.11	0.09	0.89	22.67	1002.33	2.62
37		738.61	3401.98	31442.35	2.50	-0.04	0.10	0.83	22.46	1010.26	2.78
38		736.63	3399.87	32256.39	2.30	-0.13	0.10	0.97	23.01	1010.92	2.95
39		735.49	3401.46	33962.84	1.30	0.18	0.12	1.56	25.30	1010.98	3.04
40		733.53	3400.27	35247.84	0.90	-0.06	0.13	1.15	23.73	1012.49	2.85

The field-measured salinity (Sf) ranged from 3.04 dS/m, and the modelled values (Sm) varied between 2.51 dS/m and 0.98 dS/m. The land top-layer temperatures fluctuated between 26.18 °C and 22.42 °C, and evapotranspiration rates changed between time intervals. The estimated water density ranged from 1017.66 kg/m^3 to 1000.05 kg/m^3. These figures vary based on numerous factors such as the hydrology, climate, and geology (Soler *et al.*, 2021). Changes in water depth are linked to variations in flow circulation and sedimentation (Serra *et al.*, 2002). This study shows that differences in how flow and sediment are distributed cause ongoing changes in the bottom surface, leading causing alterations in water depth and salinity. Changes in NDCI are linked to factors such as light intensity and organic matter concentration, as noted in (Shourabi *et al.*, 2023). On the other hand, salinity differences across water bodies are related to evaporation and recharge rates under local climate conditions (Suchan and Azam, 2021).

Furthermore, geological settings and the topography of the marsh bottom result in variations in water density and temperatures at the surface (Guimond and Tamborski, 2021). This variety is a clear indication of an in-depth understanding of the environmental processes that influence water salinity. The observed occurrences may be related to various, intertwined peculiarities of the complex environmental patterns in the research area. Alterations in water depth and distance from the source directly influence water renewal rates and the physical and chemical processes that produce salt accretion. This approach supports (Sun *et al.*, 2020) the claims that combining data enables us to obtain a richer view of environmental processes and phenomena (Moustafa *et al.*, 2024). Receding water depths, when far from the water source, result in poor water exchange and salt accumulation. This is related to the natural behavior of renewal processes in the hydrological system, where water on the surface contributes more to evaporation and concentration (Da De Cunha *et al.*, 2021). Increases in LST increase evapotranspiration rates and eventually lead to saltwater concentration. This relationship has been documented in various studies, and (Shokri-Kuehni *et al.*, 2017) reported that changes in climatic temperatures directly affect aquatic layer properties by prompting evaporation on hot days. The NDCI is a measure of the state of biological activity in the water and, therefore, may be indirectly connected to chemical processes in the water system. Greater biological activity can alter water properties, therewith altering the salt regime (Wang *et al.*, 2024a).

Evaluating model effectiveness and how it relates to field measurements

Figure 2 indicatesa significant linear correlation between field-measured salinity (Sf) and model-estimated salinity with remote sensing data (Sm). The r-value was 0.714, indicating that the model accounted for 71.4% of salinity variability in the water. This emphasises the model's strong capability to simulate, in particular, the general trend in salinity distribution in the water body. At the same time, differences have been observed between n-values from samples; however, these differences may indicate that standards calibration lacks standardization, e.g., sample No. 39 shows up to 8 ds/m difference between external and internal solutions. Such divergences could necessitate further improved atmospheric adjustment algorithms and a higher density of field measurements. These results agree with those of (Luo *et al.*, 2024), who also pointed out the significance of precise atmospheric adjustment to improve fineness in simulation using satellite data.

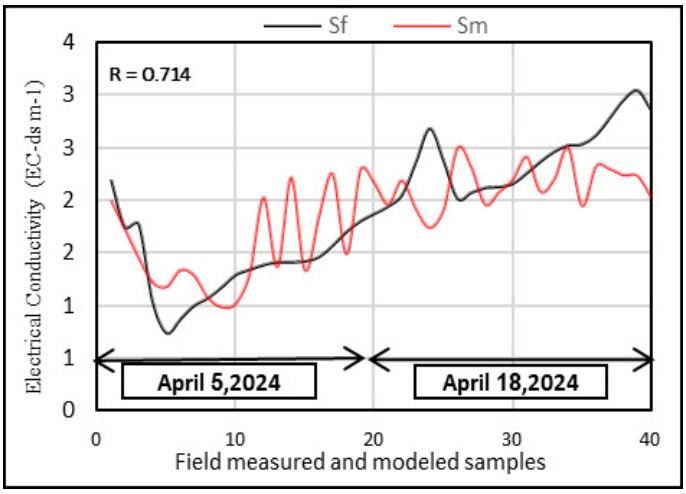

Figure 2: *Relationship between field measured (Sf) and model calculated water salinity using remote sensing (Sm).*

The highest field-measured salinity (Sf) was 3.04 ds/m, and the lowest was about 0.74 ds/m. Model-estimated salinity (Sm) ranged from 0.98 to 2.51 ds/m. The two curves black for field values and red for modelled values are mostly similar, but there are some small differences. These differences may be due to differences in remote sensing data correctness, timing of sample collection, or field conditions. The figure also shows how salinity changed between April 5 and April 18, 2024, likely because of changes in

climate or water conditions (Table 3). Combining field measurements with satellite-based models helps expand monitoring and analysis without needing as much fieldwork. This approach saves time and effort, but it further stresses the requirement to optimize the model correctness through improving atmospheric correction and calibration.

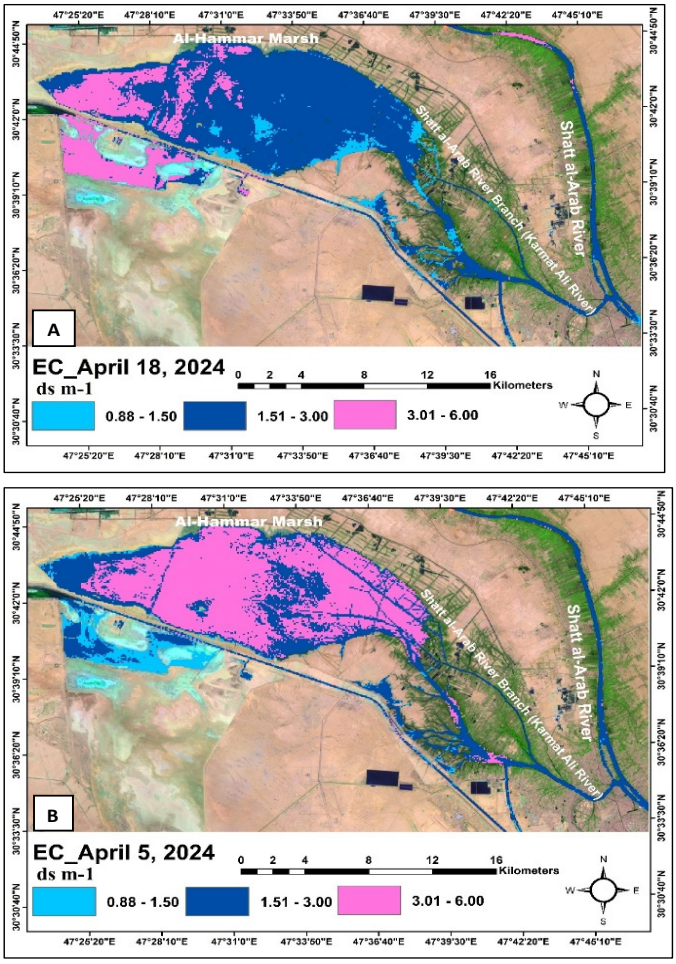

Figure 3: *Simulated spatial distribution of salt concentrations in the study area on April 5 (A) and 18th (B), 2024.*

Simulation of the spatial and temporal distribution of water salinity

Figure 3 shows the dynamic allocation of salinity in the region on 5 and 18 April 2024, indicating that salinity varied over time in Al-Himar marsh and the Karamah River along the Shatt al-Arab branch. On 5 April, water salinity ranged from 3.01 to 6.00 dS m^{-1}, with the highest concentrations in the central basin. On the other hand, the distribution of this parameter on April 18 indicates a water-mass advance and an accumulation of these values towards the end of the study area and in the basin. This variation may also occur due to changes associated with water renewal impulses, physical and chemical variations during tidal influences in the Shatt Al-Arab, the main supply, as well as environmental and transitory climatic conditions (Asadi and Alhello, 2019), (Table 3). Moreover, dispersion by a zone of low salinity (0.88–1.50 dS m^{-1}) is visible, showing that salinity decreases towards areasclose to the Shatt Al-Arab River. It is possible that, by being close to water and continually running into the ocean, salt isn't able to build up enough. On the other hand, in areas farther from the coast, higher evapotranspiration rates make the water saltier (Xin *et al.*, 2022). We have confirmed that such spatial and temporal variations result from the combination of complex physical and hydrological factors that affect the salinity regime, water flow, and solute transport in salt marshes, which are mainly driven by tidal movements, with a moderate influence from rainfall, evapotranspiration, and sea level rise. Tidal variations play a central role in plant zonation by modifying soil aeration and salt transport. They contribute to the export of large amounts of carbon and nutrients to coastal waters. Variations in surface water and groundwater temperatures affect water flow, soil conditions, and biogeochemical exchanges.

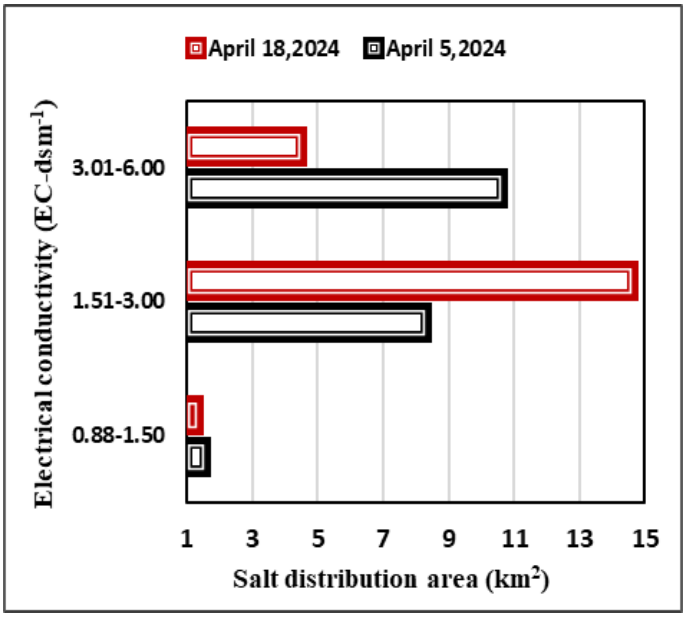

Figure 4: *The classification and distribution of salts in the study area.*

Figure 4 shows a classification of the salinity area based on ranges of electrical conductivity dividing the region into three main categories 0.88–1.50 dS m^{-1}, 1.51–3.00 dS m^{-1} and 3.01–6.00 dS m^{-1} It is observed that on April 5 there is an increased spatial coverage of the 3.01–6.00 dS m^{-1} category compared to the same category on April 18 which instead recorded a clear increase in the extent of the 1.51–3.00 dS m^{-1} category. This variation shows that the study area is very dynamic, with water salinity in Al-Hammar

marsh changing rapidly and frequently. These changes are mainly due to hydrological and hydraulic factors, as well as the direct effect of tides on water renewal in the Shatt al-Arab River, consistent with (Al-Mulla, and Al-Ali, 2015).

Difficulties and constraints of the modelling

Despite the model's success in portraying the overall trend in water salinity distribution, several shortcomings emerge from differences between field and modelled measurements. These differences may result because of elements like calibration accuracy, limited atmospheric correction data, and the low spatial and temporal resolution of the satellite imagery used (Roohi, 2024). Also, using only a few variables might miss other important influences, such as wind and sudden changes in water flow (Liu *et al*., 2020). Consequently, there is a need to adopt more improved atmospheric correction models and incorporate additional variables to enhance modelling accuracy, as noted by Sola *et al*. (2018).

Conclusions

Combining field survey measurements with satellite data has enabled a holistic approach to the aquatic system, revealing spatial and temporal differences in its properties. The correlation coefficient between field observations and values predicted by the mathematical model is 0.714, indicating that the model may explain up to 71.4% of the variation in water salinity. The atmosphere-correction procedures should be further developed, and the density of measurement points should be increased. Salinity is influenced by physical and climatic conditions. The further from the source, the shallower and slower to renew water becomes, and so salt builds up.

In the meantime, warmer surface heat levels and higher precipitation rates result in greater salt content. Also, biological activity (as denoted by the NDCI index) is involved in chemical interactions as well as salt distribution. For the 5–18 April 2024 simulations, the time-space variability of the salinity distribution between source-proximal and distal areas posed a dynamic challenge for field versus modelled estimates due due to constraints in atmospheric correction and satellite constraints in space and time. This demonstrates the need to combine field data with RS information to make better decisions in water resources.

Future recommendations and practical approaches

The results imply that the field database should be extended both in area and in data detail, enabling us to recalibrate the model and improve its accuracy. It is also recommended to use multispectral sensing technology, including radar and infrared, to identify slight variations in water state. In addition, dynamic models including minute changes in natural factors are needed to provide more accurate salinity forecasts under the continuing effect of climate change. This evidence are important both from the point of view of scientific model development, but also for policy-relevant applications in water resources management and environmental planning, especially in vulnerable areas with strong reactions to climatic variability.

Acknowledgement

The authors would like to thank the College of Marine Sciences and the College of Agriculture / University of Basra for their support and for providing access to their laboratories and facilities, which helped complete the research.

Novelty Statement

This study combines dimensional analysis and remote sensing data to create a predictive model for tracking salinity changes in the Hammar Marsh–Shatt Al-Arab system. This method offers a new way to model water movement and monitor water quality in changing river and estuary environments.

Author's Contribution

Forqan Khalid Al-Daraji, Husam Hasan Abdulaali, Yousif sh. J. Al-Jorani, and Mu'ayyad H. M. Al-Bahadli: handled the materials, collected the data, and carried out the analysis. The first draft of the manuscript focused on simulating and predicting hydrodynamic changes in water salinity in the Hammar Marsh and Shatt Al-Arab River using dimensional analysis and remote sensing. Husam Hasan Abdulaali revised the scientific content, improved the language and presentation, and gave advice to make the research suitable for peer-reviewed journals. All authors reviewed earlier versions of the chapter and approved the final version. All authors participated in the design and preparation of the study.

Funding declaration
The authors declare that no funds, grants, or other support were received during the preparation of this manuscript.

Generative AI and AI assisted technology statement
The authors declare that no generative AI and AI assisted technology was used in the creation of this manuscript.

Statement of conflict of interest
The authors have declared no conflict of interest.

References

Adamo, N., Al-Ansari, N., Sissakian, V.K., Laue, J. and Knutsson, S., 2018. The future of the tigris and euphrates water resources in view of climate change. J. Earth Sci. Geotech. Engin., 8: 1792–9660.

Ahmed, W., Mohammed, S., El-Shazly, A. and Morsy, S., 2023. Tigris River water surface quality monitoring using remote sensing data and GIS techniques. Egypt. J. Remote Sens. Space Sci., 26: 816–825. https://doi.org/10.1016/j.ejrs.2023.09.001

Al-Daraji, F.K., Ndewi, D.R. and Al-Shammari, H.M., 2024. Modeling water supply in adjacent areas of shatt Al-Arab River in Southern Iraq using geomatics techniques. IOP Conf. Ser. Earth Environ. Sci., 1371. https://doi.org/10.1088/1755-1315/1371/8/082027

Al-Daraji, F.K., Ndewi, D.R. and Al-Shammari, H.M., 2025. Modeling and analysis of land surface temperature variations in Basrah Governorate, Iraq, using remote sensing data and geomatics techniques. Springer Proceedings in Earth and Environmental Sciences, Part F3200, pp. 89–104. https://doi.org/10.1007/978-3-031-57054-4_7

Al-Jawad, M.M., Nedawi, D.R. and Al-Manssory, F.Y., 2018. Studies on salt distribution in the Northern Part of Shatt al-Arab Waterway, Iraq. pp. 146–151.

Al-Jiburi, H.K. and Al-Basrawi, N.H., 2009. Hydrogeoleogy. Iraqi Bull. Geol. Min. Special Issue, pp. 77–91.

Al-Khakani, E.T., Al-Janabi, W.F., Sa'ad, R.Y. and Al-Kazaali, H.M., 2018. Using landsat 8 OLI data to predict and mapping soil salinity for part of An-Najaf governorate. Ecol. Environ. Conserv., 24: 572–578.

Al-Khalidi, J., Dima, M. and Stefan, S., 2018. Large-scale modes impact on Iraq climate variability. Theor. Appl. Climatol., 133: 179–190. https://doi.org/10.1007/s00704-017-2180-z

Al-Mahmood, H.K. and Mahmood, A.B., 2021. Effect of Karun River on the salinity status in the Shatt Al-Arab River, Basrah- Iraq. Mesopot. J. Mar. Sci., 34: 13–26. https://doi.org/10.58629/mjms.v34i1.42

Al-Mulla, S.T. and Al-Ali, A. K. 2015. Geomatic study of Shatt Al-Arab delta, southern Iraq. Marsh Bull., 10(1).

Alqasemi, A.S., Ibrahim, M., Fadhil Al-Quraishi, A.M., Saibi, H., Al-Fugara, A. and Kaplan, G., 2021. Detection and modeling of soil salinity variations in arid lands using remote sensing data. Open Geosci., 13: 443–453. https://doi.org/10.1515/geo-2020-0244

Al-Salihi, Z.A., Kamel, A.H. and Abdulhameed, I.M., 2024. Effect of climate changes on water resources in Iraq: A review study. AIP Conf. Proc., 3009. https://doi.org/10.1063/5.0190474

Ansari, M., Knudby, A. and Homayouni, S., 2025. River salinity mapping through machine learning and statistical modeling using Landsat 8 OLI imagery. Adv. Space Res., https://doi.org/10.1016/j.asr.2025.03.037

Asadi, S.A.R. and Alhello, A.A., 2019. General assessment of Shatt Al-Arab River, Iraq. Int. J. Water, 13: 360. https://doi.org/10.1504/IJW.2019.106049

Borovskaya, R., Krivoguz, D., Chernyi, S., Kozhurin, E., Khorosheltseva, V. and Zinchenko, E., 2022. Surface water salinity evaluation and identification for using remote sensing data and machine learning approach. J. Mar. Sci. Eng., 10. https://doi.org/10.3390/jmse10020257

Chen, S. and Hu, C., 2017. Estimating sea surface salinity in the northern Gulf of Mexico from satellite ocean color measurements. Remote Sens. Environ., 201: 115–132. https://doi.org/10.1016/j.rse.2017.09.004

Da De Cunha, C.L.N., Scudelari, A.C., De Sant'Ana, D.O., Luz, T.E.B. and Da Pinheiro, M.K.R., 2021. Effects on circulation and water renewal due to the variations in the river flow and the wind in a Brazilian estuary lagoon complex. Rev. Ambiente Água, 16: e2600. https://doi.org/10.4136/ambi-agua.2600

Danboos, A., Sharil, S., Hamzah, F.M., Yafouz, A., Huang, Y.F., Ahmed, A.N. and El-Shafie,

A., 2023. Water budget-salt balance model for calculating net water saving considering different non-conventional water resources in agricultural process. Heliyon, 9(4). https://doi.org/10.1016/j.heliyon.2023.e15274

Guimond, J. and Tamborski, J., 2021. Salt Marsh Hydrogeology: A review. Water, 13: 543. https://doi.org/10.3390/w13040543

Haleem, A. and Al-Muhyi, A., 2018. The challenges facing Shatt Al-Arab River in present and future. Marshbulltin, 2: 1–22.

Hamdan, A.N., Najm, A.T. and Abbas, A.A., 2018. Flow simulation of Shatt Al-Arab River by HEC-RAS 5.0. 3. Int. J. Adv. Mech. Civil Engin., 15(1): 31-36.

Hamdan, A.N.A., Al-Mahdi, A.A.J. and Mahmood, A.B., 2020. Modeling the Effect of Sea Water Intrusion into Shatt Al-Arab River (Iraq). J. Univ. Babylon Engin. Sci., 28: 210–224.

Harmel, R.D., Preisendanz, H.E., King, K.W., Busch, D., Birgand, F. and Sahoo, D., 2023. A review of data quality and cost considerations for water quality monitoring at the field scale and in small watersheds. Water (Switzerland), 15: 1–19. https://doi.org/10.3390/w15173110

Jia, P., He, W., Hu, Y., Liang, Y., Liang, Y., Xue, L. and Zhao, X., 2024. Inversion of coastal cultivated soil salt content based on multi-source spectra and environmental variables. Soil Till. Res., 241: 106124. https://doi.org/10.1016/j.still.2024.106124

Li, W., Liu, J., Bao, N., Mao, X., Mao, Y., Fu, Y., Cao, W., Huang, J., and Zhao, Z., 2021. Salinity monitoring at saline sites with visible–near-infrared spectral data. Minerals, 11: 1086. https://doi.org/10.3390/min11101086

Liu, S., Ye, Q., Wu, S. and Stive, M.J.F., 2020. Wind effects on the water age in a large shallow lake. Water, 12: 1246. https://doi.org/10.3390/w12051246

Luo, B., Minnett, P.J. and Jia, C., 2024. Improving atmospheric correction algorithms for sea surface skin temperature retrievals from moderate-resolution imaging spectroradiometer using machine learning methods. Remote Sens., 16: 4555. https://doi.org/10.3390/rs16234555

Mohamed, A.R.M., Al-Saboonchi, A.A. and Raadi, F.K., 2016. Ecological assessment of East Hammar marsh, Iraq using a number of ecological guides. J. King Abdulaziz Univ. Mar. Sci., 26: 11–22. https://doi.org/10.4197/Mar.26-2.2

Moustafa, M.Z., Ji, Z.G. and Hamrick, J., 2024. Impacts of freshwater sources on salinity structure in a large, shallow estuary. Environments, 11: 72. https://doi.org/10.3390/environments11040072

Mukhamediev, R.I., Merembayev, T., Kuchin, Y., Malakhov, D., Zaitseva, E., Levashenko, V., Popova, Y., Symagulov, A., Sagatdinova, G., and Amirgaliyev, Y., 2023. Soil salinity estimation for south kazakhstan based on SAR Sentinel-1 and Landsat-8,9 OLI data with machine learning models. Remote Sens., 15. https://doi.org/10.3390/rs15174269

Pałas, K.W. and Zawadzki, J., 2020. Sentinel-2 imagery processing for tree logging observations on the bialowieza forest world heritage site. Forests, 11. https://doi.org/10.3390/f11080857

Phull, A.M. and Babar, M.M., 2012. Summulation of soil wetting pattern of subsurface. Sixteenth International Water Technology Conference, IWTC 16 2012, Istanbul, Turkey, 1–11.

Qadra, L.Z., 2020. Study of the water quality in the Shatt Al-Arab River Southern of Iraq: A review. J. Engin. Sustain. Dev., 24: 24–36. https://doi.org/10.31272/jeasd.conf.1.3

Racetin, I., Krtalic, A., Srzic, V. and Zovko, M., 2020. Characterisation of short-term salinity fluctuations in the Neretva River Delta situated in the southern Adriatic Croatia using Landsat-5 TM. Ecol. Indicat., 110: 105924. https://doi.org/10.1016/j.ecolind.2019.105924

Roohi, M., 2024. Enhancing the quality of satellite images for estimating the water body. JSM Environ. Sci. Ecol., 12: 1–9. https://doi.org/10.47739/2333-7141.environmentalscience.1088

Sahbeni, G., 2021. Soil salinity mapping using Landsat 8 OLI data and regression modeling in the Great Hungarian Plain. SN Appl. Sci., 3: 1–13. https://doi.org/10.1007/s42452-021-04587-4

Saleh, A.M., 2017. Evaluation of different soil salinity mapping using remote sensing indicators and regression techniques, Basrah, Iraq. J. Am. Sci., 13: 85–97.

Serra, T., Colomer, J., Gacia, E., Soler, M. and Casamitjana, X., 2002. Effects of a turbid hydrothermal plume on the sedimentation rates in a karstic lake. Geophys. Res. Lett., 29: 25-31. https://doi.org/10.1029/2002GL015368.

Shokri-Kuehni, S.M.S., Vetter, T., Webb, C. and Shokri, N., 2017. New insights into saline water evaporation from porous media: Complex interaction between evaporation rates, precipitation, and surface temperature. Geophys. Res. Lett., 44: 5504–5510. https://doi.org/10.1002/2017GL073337

Shourabi, K.Y., Niksokhan, M.H. and Roozitalab, S., 2023. Inundation and water quality assessment of the Karun river before and after flooding using remote sensing,

Sissakian, V.K., Shihab, A.T., Al-Ansari, N. and Knutsson, S., 2014. Al-Batin Alluvial Fan, Southern Iraq. Engineering, 6: 699–711. https://doi.org/10.4236/eng.2014.611069

Smaysim, L.A. and Slewa, S.L., 2014. Nomination dossier for inscription of the property on the world heritage list - the ahwar of Southern Iraq and the relict landscape of the mesopotamian cities. TAPPI Journal, 13.

Sola, I., García-Martín, A., Sandonís-Pozo, L., Álvarez-Mozos, J., Pérez-Cabello, F., González-Audícana, M. and Montorio-Llovería, R., 2018. Assessment of atmospheric correction methods for Sentinel-2 images in Mediterranean landscapes. Int. J. Appl. Earth Observ. Geoinf., 73: 63–76. https://doi.org/10.1016/j.jag.2018.05.020

Soler, M., Serra, T., Folkard, A. and Colomer, J., 2021. Hydrodynamics and sediment deposition in turbidity currents: Comparing continuous and patchy vegetation canopies, and the effects of water depth. J. Hydrol., 594: 125750. https://doi.org/10.1016/j.jhydrol.2020.125750

Suchan, J. and Azam, S., 2021. Determination of evaporative fluxes using a bench-scale atmosphere simulator. Water (Switzerland), 13. https://doi.org/10.3390/w13010084

Sun, J., Liu, L., Lin, J., Lin, B. and Zhao, H., 2020. Vertical water renewal in a large estuary and implications for water quality. Sci. Total Environ., 710: 135593. https://doi.org/10.1016/j.scitotenv.2019.135593

Tajudin, N., Ya'acob, N., Ali, D.M. and Adnan, N.A., 2021. Soil moisture index estimation from Landsat 8 images for prediction and monitoring landslide occurrences in Ulu Kelang, Selangor, Malaysia. Int. J. Elect. Comp. Engin., 11: 2101–2108. https://doi.org/10.11591/ijece.v11i3.pp2101-2108

Van Zandwijk, A.E., Monji, F., Mento, L., Van Opstal, R., Mahdi, K. and Snertlage, J., 2021. Water and Saline Agriculture in Central-Southern Iraq.

Vijayan, V., Dwivedi, D.K. and Roy, P.S., 2010. Remote sensing applications.

Wang, F. and Xu, Y.J., 2015. Remote sensing to predict estuarine water salinity Chapter 8 remote sensing to predict estuarine water salinity.

Wang, W., Zhang, D., Kong, H., Zhang, G., Shen, F. and Huang, Z., 2024a. Effects of salinity accumulation on physical, chemical, and microbial properties of soil under rural domestic sewage irrigation. Agronomy 14: 514. https://doi.org/10.3390/agronomy14030514

Wang, X., Fan, G., Ding, R., Jin, H., Hao, W. and Tao, M., 2024b. Water salinity sensing with UAV-mounted IR-UWB radar. ACM Transactions on Sensor Networks, 20. https://doi.org/10.1145/3633515

Wang, F. and Xu, Y.J., 2011. Remote Sensing to Predict Estuarine Water Salinity. Chapter 8: Remote sensing to predict estuarine water salinity. https://doi.org/10.1201/b11702-7

Xin, P., Wilson, A., Shen, C., Ge, Z., Moffett, K.B., Santos, I.R., Chen, X., Xu, X., Yau, Y.Y., Moore, W. and Li, L., 2022. Surface water and groundwater interactions in salt marshes and their impact on plant ecology and coastal biogeochemistry. Rev. Geophys., 60: e2021RG000740. https://doi.org/10.1029/2021RG000740

Zhao, J., Temimi, M. and Ghedira, H., 2017. Remotely sensed sea surface salinity in the hyper-saline Arabian Gulf: Application to landsat 8 OLI data. Estuarine, Coast. Shelf Sci., 187: 168–177. https://doi.org/10.1016/j.ecss.2017.01.008